Research Article | Vol. 8, No. 1 | 1 Jan 2018 | OPTICAL MATERIALS EXPRESS 50
Optical Materials EXPRESS

Terahertz integrated device: high-Q silicon dielectric resonators

JINGYA XIE, XI ZHU, XIAOFEI ZANG, QINGQING CHENG, LIN CHEN, AND YIMING ZHU*

Terahertz Technology Innovation Research Institute, Shanghai Key Lab of Modern Optical System, and Engineering Research Center of Optical Instrument and System, Ministry of Education, Terahertz Spectrum and Imaging Cooperative Innovation Center, University of Shanghai for Science and Technology, No. 516 JunGong Road, Shanghai 200093, China
**ymzhu@usst.edu.cn*

Abstract: We design, fabricate, and characterize the terahertz integrated resonators on the silicon platform. Based on mode analysis and selection, the high-Q feature of resonators made of low-loss high-resistivity Si material is achieved due to the excitation of the whispering gallery mode on waveguide-coupled single-mode racetrack rings and disk cavities. The experimental results demonstrate that the Q-factor can reach up to 2839 at 218.345 GHz, which is significantly improved compared with conventional THz cavities. These high Q-factor integrated resonators can be used as on-chip terahertz ultrasensitive sensors and as terahertz functional integrated circuits.

OCIS codes: (230.3120) Integrated optics devices; (230.5750) Resonators.

References and links

1. B. Ferguson and X. C. Zhang, "Materials for terahertz science and technology," Nat. Mater. **1**(1), 26–33 (2002).
2. M. Tonouchi, "Cutting-edge terahertz technology," Nat. Photonics **1**(2), 97–105 (2007).
3. W. Bogaerts, P. D. Heyn, T. V. Vaerenbergh, K. D. Vos, S. K. Selvaraja, T. Claes, P. Dumon, P. Bienstman, D. V. Thourhout, and R. Baets, "Silicon microring resonators," Laser Photonics Rev. **6**(1), 47–73 (2012).
4. V. S. Ilchenko and A. B. Matsko, "Optical resonators with whispering-gallery modes-part II: applications," IEEE J. Sel. Top. Quantum Electron. **12**(1), 15–32 (2006).
5. Y. Yang, J. Ward, and S. N. Chormaic, "Quasi-droplet microbubbles for high resolution sensing applications," Opt. Express **22**(6), 6881–6898 (2014).
6. J. Xie, L. Zhou, Z. Zou, J. Wang, X. Li, and J. Chen, "Continuously tunable reflective-type optical delay lines using microring resonators," Opt. Express **22**(1), 817–823 (2014).
7. J. Xie, L. Zhou, X. Sun, Z. Zou, L. Lu, H. Zhu, X. Li, and J. Chen, "Selective excitation of microring resonances using a pulley-coupling structure," Appl. Opt. **53**(5), 878–884 (2014).
8. S. S. Harsha, N. Laman, and D. Grischkowsky, "High-Q terahertz Bragg resonances within a metal parallel plate waveguide," Appl. Phys. Lett. **94**(9), 091118 (2009).
9. E. S. Lee, S. G. Lee, C. S. Kee, and T. I. Jeon, "Terahertz notch and low-pass filters based on band gaps properties by using metal slits in tapered parallel-plate waveguides," Opt. Express **19**(16), 14852–14859 (2011).
10. A. L. Bingham and D. Grischkowsky, "High Q, one-dimensional terahertz photonic waveguides," Appl. Phys. Lett. **90**(9), 091105 (2007).
11. V. Astley, B. McCracken, R. Mendis, and D. M. Mittleman, "Analysis of rectangular resonant cavities in terahertz parallel-plate waveguides," Opt. Lett. **36**(8), 1452–1454 (2011).
12. Z. Gao, L. Shen, X. Zheng, J. Wu, T. Yang, and D. Yang, "Terahertz plasmonic microcavity with high quality factor and ultrasmall mode volume," Plasmonics **8**(2), 319–324 (2013).
13. L. Chen, N. Xu, L. Singh, T. Cui, R. Singh, Y. Zhu, and W. Zhang, "Defect-induced Fano resonances in corrugated plasmonic metamaterials," Adv. Optical Mater. **5**(8), 1600960 (2017).
14. L. Chen, Y. Wei, X. Zang, Y. Zhu, and S. Zhuang, "Excitation of dark multipolar plasmonic resonances at terahertz frequencies," Sci. Rep. **6**(1), 22027 (2016).
15. N. Xu, R. Singh, and W. Zhang, "High-Q lattice mode matched structural resonances in terahertz metasurfaces," Appl. Phys. Lett. **109**(2), 021108 (2016).
16. J. Xie, X. Zhu, X. Zang, Q. Cheng, Y. Ye, and Y. Zhu, "High extinction ratio electromagnetically induced transparency analogue based on the radiation suppression of dark modes," Sci. Rep. **7**(1), 11291 (2017).
17. S. Preu, H. G. L. Schwefel, S. Malzer, G. H. Döhler, L. J. Wang, M. Hanson, J. D. Zimmerman, and A. C. Gossard, "Coupled whispering gallery mode resonators in the Terahertz frequency range," Opt. Express **16**(10), 7336–7343 (2008).

#312656 https://doi.org/10.1364/OME.8.000050
Journal © 2018 Received 3 Nov 2017; revised 5 Dec 2017; accepted 6 Dec 2017; published 8 Dec 2017

Optical Materials EXPRESS

18. D. W. Vogt and R. Leonhardt, "Terahertz whispering gallery mode bubble resonator," Optica **4**(7), 809–812 (2017).
19. D. W. Vogt and R. Leonhardt, "Fano resonances in a high-Q terahertz whispering-gallery mode resonator coupled to a multi-mode waveguide," Opt. Lett. **42**(21), 4359–4362 (2017).
20. P. A. George, C. Manolatou, F. Rana, A. L. Bingham, and D. R. Grischkowsky, "Integrated waveguide-coupled terahertz microcavity resonators," Appl. Phys. Lett. **91**(19), 191122 (2007).
21. W. Deal, X. B. Mei, K. Leong, S. Sarkozy, and R. Lai, "THz monolithic integrated circuits using InP high electron mobility transistors," IEEE Trans. THz Sci. Technol. **1**(1), 25–32 (2011).
22. J. Dai, J. Zhang, W. Zhang, and D. Grischkowsky, "Terahertz time-domain spectroscopy characterization of the far-infrared absorption and index of refraction of high-resistivity, float-zone silicon," J. Opt. Soc. Am. B **21**(7), 1379–1386 (2004).
23. C. M. Yee and M. S. Sherwin, "High-Q terahertz microcavities in silicon photonic crystal slabs," Appl. Phys. Lett. **94**(15), 154104 (2009).
24. A. Patrovsky and K. Wu, "Substrate integrated image guide (SIIG)-a planar dielectric waveguide technology for millimeter-wave applications," IEEE Trans. THz Sci. Technol. **54**(6), 2872–2879 (2006).
25. A. Malekabadi, S. A. Charlebois, D. Deslandes, and F. Boone, "High resistivity silicon dielectric ribbon waveguide for single-mode low-loss propagation at F/G-bands," IEEE Trans. THz Sci. Technol. **4**(4), 447–453 (2014).
26. C. Yeh, F. Shimabukuro, and P. H. Siegel, "Low-loss terahertz ribbon waveguides," Appl. Opt. **44**(28), 5937–5946 (2005).
27. N. Ranjkesh, M. Basha, A. Taeb, A. Zandieh, S. Gigoyan, and S. Safavi-Naeini, "Silicon-on-glass dielectric waveguide—Part I For millimeter-wave integrated circuits," IEEE Trans. THz Sci. Technol. **5**(2), 268–279 (2015).
28. N. Ranjkesh, M. Basha, A. Taeb, and S. Safavi-Naeini, "Silicon-on-glass dielectric waveguide—Part II: For THz applications," IEEE Trans. THz Sci. Technol. **5**(2), 280–287 (2015).
29. H. Zhu, Q. Xue, J. Hui, and S. Pang, "A 750-1000 GHz H-plane dielectric horn based on silicon technology," IEEE Trans. Antenn. Propag. **64**(12), 5074–5083 (2016).
30. P. K. Tien, "Light waves in thin films and integrated optics," Appl. Opt. **10**(11), 2395–2413 (1971).
31. D. K. Sparacin, S. J. Spector, and L. C. Kimerling, "Silicon waveguide sidewall smoothing by wet chemical oxidation," J. Lightwave Technol. **23**(8), 2455–2461 (2005).
32. S. C. Hung, E. Z. Liang, and C. F. Lin, "Silicon waveguide sidewall smoothing by KrF excimer laser reformation," J. Lightwave Technol. **27**(7), 887–892 (2009).
33. A. Yariv, "Universal relations for coupling of optical power between microresonators and dielectric waveguides," Electron. Lett. **36**(4), 321–322 (2000).

1. Introduction

Terahertz (THz) wave is a kind of electromagnetic wave, typically within the frequency range of 0.1-10 THz, between microwave and infrared radiation regions [1]. It has attracted considerable attention for its high potential in high-speed communication, security imaging, medical imaging, and molecular spectroscopy [2]. Similar to optical devices, in terahertz regions, small cavities with high quality (Q) factor are fundamental to the implementation of compact spectral switches and filters, optical delay lines, lasers and sensors [3–7]. Lots of work has been made in realizing THz resonators, including metal parallel plate waveguides [8–11], plasmonics [12–14], metasurfaces [15, 16], and dielectric cavities [17–19], yet most of the solutions suffer from bulky size, which prevent further integration. The planar resonator is advantageous in a sense that it can be monolithically fabricated and integrated with the active components such as the source and detector.

One possible solution for THz integrated resonators is CMOS-based metal waveguide [20]. However, metal devices have large attenuations caused by conductor loss in THz, which are not suitable for high-Q THz applications [21]. High resistivity silicon is found to be an effective material for THz dielectric waveguide integration, for its lower dispersion and loss characteristics [22]. Recently, integrated dielectric silicon photonic crystal slabs are proposed [23]. However, since fabrication of 3-D photonic crystal structures is still a difficult process, it is harder to reduce the scattering loss of holes and increase the Q factor. Besides the photonic crystal waveguide, various THz silicon waveguides were fabricated and measured, such as substrate integrated image guide (SIIG) [24], ribbon waveguide [25, 26], silicon-on-glass (SOG) waveguide [27, 28] and slab waveguide [29]. These results demonstrated the low transmission loss characteristics of silicon waveguides. In general, previous work shows great

Optical Materials EXPRESS

potential of silicon techniques in integrated THz resonator cavities, yet the Q factor is to be enhanced.

Based on the development of THz silicon waveguide, this paper reports the achievement of all-silicon integrated cavities with high-Q factors. Compared with a very recent terahertz resonator based on whispering gallery mode bubble resonator [18, 19], the Q-factor of our proposed resonator has reached 2839, which is much improved by designing resonance mode and reducing cavity loss. Both racetrack rings and whispering gallery mode cavities are designed and fabricated in the same wafer. We use disk structure to produce the whispering gallery mode, which is suitable for planar integrated device. Straight dielectric ridge waveguides are used for coupling with metal rectangular waveguides and exciting the cavity modes.

2. Device design and fabrication

Figure 1(a)-1(b) shows the schematic drawing of the disk cavity, racetrack ring, and cross-sectional view of waveguides, respectively. The device is based on ridge-type waveguides, where the ridge is 500 μm wide (W) and 340 μm high (H), over the slab with thickness of 130 μm (h). Figure 1(c) shows the cross-sectional view of ridge-type waveguides. The radius of the racetrack ring is r = 3.25 mm. The coupling length (L) is 1 cm and the gap (g) is 50 μm. The radius of the disk is r = 3 mm. Its coupling gap is the same as that of racetrack ring. The electromagnetic (EM) wave is coupled into and out of the device through straight waveguides. Integrated cavities are placed nearby the straight waveguides to excite the cavity modes. The cavities are fabricated in the same high-resistivity Si wafer. The wafer is 470-μm-thick and double-side polished. AZ4620 photoresist was spin-coated and patterned using 365-nm standard photolithography. Then silicon is etched with a depth of 340 μm from front side by inductively coupled plasma (ICP) process. The 130 μm thick slab layer is formed as a holder for the ridge waveguide. Figure 1(d)-1(f) show the optical images and zoom-in view of the disk cavity, and racetrack ring, cross-sections of wafer, respectively.

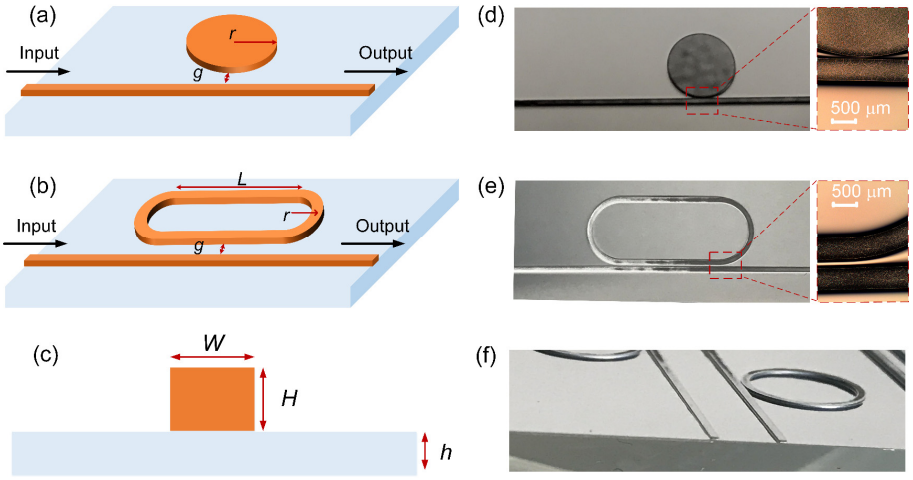

Fig. 1. Schematic illustration of (a) disk cavity structure, (b) racetrack ring cavity structure, and (c) cross-sectional view of waveguides. Optical microscope images of the fabricated sample of (d) disk cavity, (e) racetrack ring cavity, and (f) cross-sections of wafer.

The resonance Q factor is determined by the field attenuation per round trip in the cavity, which is related to the waveguide propagation loss. According to the analytical model proposed by Tien [30], the waveguide scattering loss (dB/cm) can be defined as

Optical Materials EXPRESS

$$\alpha_s = \frac{4\sigma^2 h^2}{\beta(r+2/p)} = \frac{\sigma^2 k_0^2 h}{\beta} \cdot \frac{E_s^2}{\int E^2 dx} \cdot \Delta n^2 \tag{1.1}$$

where k_0 is the free space wavenumber, β is modal propagation constant, σ is the interface roughness, r is the waveguide thickness, and Δn is the difference between the refractive indices of the guiding and cladding layers, while h and p represent the transverse propagation constants in the guide and cladding, respectively. It can be seen from the equation that loss is proportional to the normalized electric field intensity $E_s^2 / \int E^2 dx$ at the guide-cladding interface as well as the square magnitude of interface roughness σ. It should be noted that the loss is becoming larger in the long wavelength regime, for the mode is much less confined, and the interaction between electric field and rough surface is more significant.

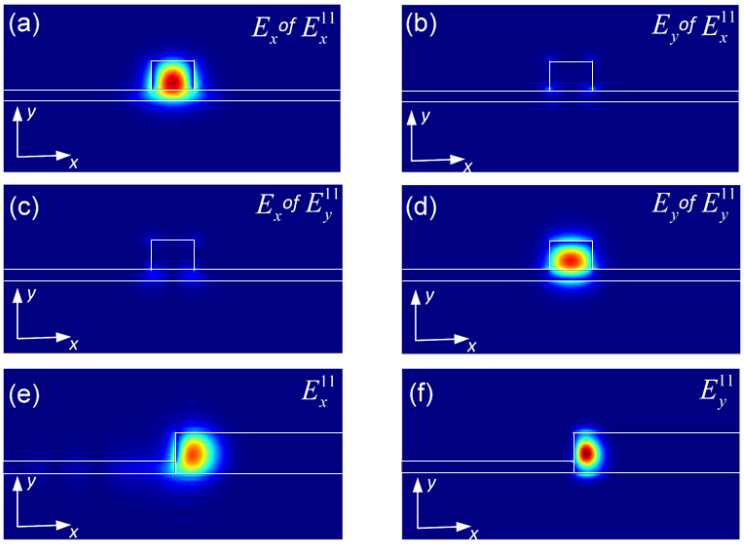

Fig. 2. Dominant transverse electric field component of distribution of waveguides. (a) E_x of E_x^{11} mode, (b) E_y of E_x^{11} mode, (c) E_x of E_y^{11} mode, (d) E_y of E_y^{11} mode. Simulated $|E|^2$ patterns of the two lowest radial order whispering gallery modes (WGMs) (e) E_x^{11} and (f) E_y^{11}.

Besides the direct influence of fabrication roughness over the scattering loss [31, 32], the mode overlap with the roughness also affects the scattering loss. Hence, we analyzed the modes of the dielectric waveguides and disk cavities in numerical calculations by solving Maxwell's equations based on the finite element method (FEM). The high-resistivity Si has a dielectric constant of ε_r = 11.7 and a resistivity of more than 5 $k\Omega\cdot cm$ (corresponding to the refractive index of 3.4205 and a very low material absorption of about 0.025 cm^{-1}). The large index contrast between the Si channel and the surrounding air results in a strong field confinement inside the Si channel. The first two propagating modes of the silicon waveguide with designed dimensions are E_x^{11} and E_y^{11}, respectively. Figures 2(a)-2(d) show the distributions of the dominant transverse electric field components of E_x^{11} and E_y^{11} modes at 200 GHz, respectively. Results demonstrate that for E_x^{11} mode, the transverse dominant component of the electric field is in x-direction, while the other transverse component of the electric field is negligible except for the corners of the guiding channel. For E_y^{11} modes, the

Optical Materials EXPRESS

dominant component of the electric field is in *y*-direction. The normalized electric field intensity $N = E_s^2 / \int E^2 dx$ at the 2 μm top interface (corresponding to the assumed top surface roughness) is shown in Fig. 3(a). The results show that E_y^{11} mode has strong interaction with the top surface roughness, leading to a higher scattering loss. The normalized electric field intensity N of E_y^{11} mode has larger variation, when the height of waveguide changed. The normalized electric field intensity at the 2 μm sidewall interface (corresponding to our fabrication edge roughness) is shown in Fig. 3(b). The E_x^{11} mode has strong interaction with the sidewall roughness, which is more affected by the width of waveguide. The modes supported in the rings/racetrack rings are the same as straight waveguides, with minor change from the bending radius.

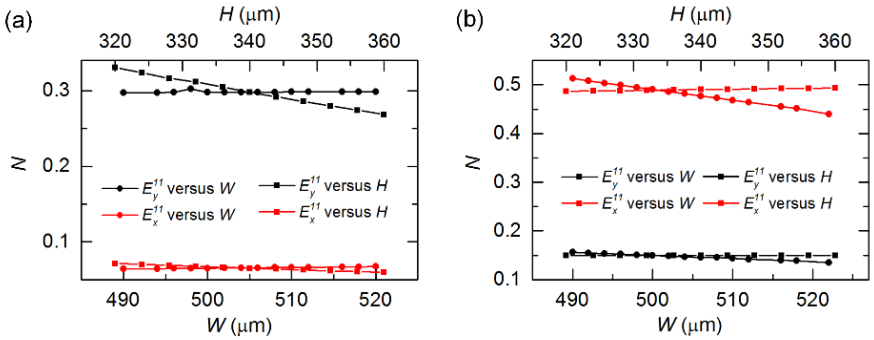

Fig. 3. The normalized electric field intensity of (a) the top surface, (b) the sidewalls.

Disk resonators possess whispering gallery modes (WGMs) which are located only around the disk rim. Figure 2(e) and 2(f) show the simulated $|E|^2$ patterns of the two lowest radial order whispering gallery modes (WGMs) of E_x^{11} and E_y^{11} modes. There is no inner sidewall in disks compared to rings, leading to the lower scattering loss of E_x^{11} mode.

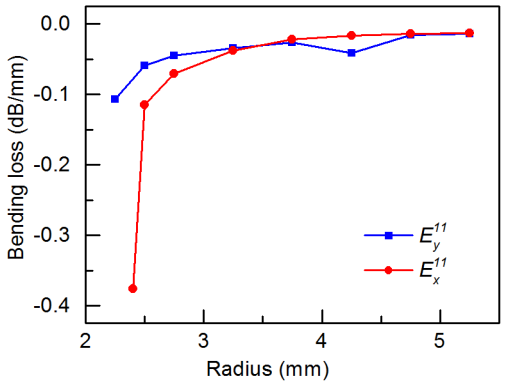

Fig. 4. Bending loss of waveguide at various radius for E_x^{11} and E_y^{11} mode.

Apart from the scattering loss, bending radiation loss is another source of the waveguide propagation loss. The loss simulations of ideal bending waveguide (without surface roughness) at various radius are shown in Fig. 4. The simulated frequency is 189.4 GHz. The propagation losses of both E_x^{11} and E_y^{11} modes are increased with the reducing of radius. Hence, there is a trade-off between the resonator size and loss. It also can be seen that, in our

Optical Materials EXPRESS

waveguide structure, E_x^{11} mode has larger loss than E_y^{11} mode at small radius. The relatively large loss of E_x^{11} mode is due to the thick silicon waveguide and small bending. Usually a wider waveguide is used for the E_x^{11} mode to get a low propagation loss.

3. Experimental results

We used the Agilent N5227A PNA network analyzer and a set of WR-5.1 140–220 GHz VNA extenders to characterize the device transmission performances. The experimental setup is shown in Fig. 5. The two VDI extenders are connected to the network analyzer with IF and RF cables. After the calibration, EM wave is coupled into the device under test from the left waveguide port. The polarization is optimized for the E_y^{11} mode through proper levelness setting of the pedestal. The output wave power is coupled from the right waveguide port and finally detected by the network analyzer. The frequency measurement precision is set to be 2 MHz. To characterize the electromagnetic responses of E_x^{11} mode, the rectangular waveguide ports need to be rotated by 90°, to ensure the consistent polarization.

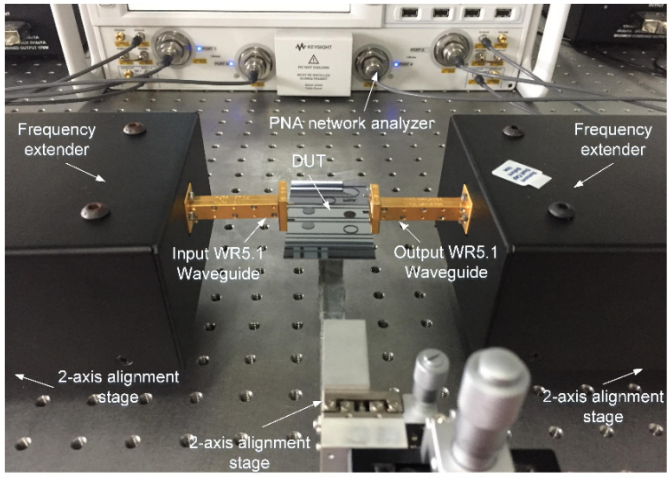

Fig. 5. Experimental setup for THz integrated cavities' measurements. DUT: device under test.

To investigate the whispering gallery modes (WGM) in integrated THz device, we first fabricated and characterized the disk resonators. The incident wave is confined inside the cavity due to a series of total internal reflections by the outside polished surface. Figure 6(a) visualize the measured transmission spectrum response for the E_x^{11} mode. The variation in the resonance extinction ratio (ER) is clearly discerned. The device insertion loss is measured to be ~8 dB (off resonance). The length of the bus waveguide is 4 cm. The coupling loss is ~3 dB/facet and the propagation loss along the bus waveguide is about ~2 dB. Resonance occurs when the wavelength satisfies $m\lambda = n_{eff} L$ (m is an integer). Therefore, n_{eff} can be deduced from the resonance wavelength for a given m (estimated from simulation). The power transfer function of the resonator is given by [33]

$$\left|H(f)\right|^2 = \left|\frac{t - ae^{-j\beta L}}{1 - ate^{-j\beta L}}\right|^2 \tag{1.2}$$

where $\beta = 2\pi n_{eff} f / c$ is the propagation constant of the resonator waveguide, f is the frequency, n_{eff} is the waveguide effective index, L is the perimeter of the resonator, t is the

Optical Materials EXPRESS

coupling coefficient, and a is the field attenuation per round trip in the cavity. At certain resonance frequency, t and a can be extracted from the corresponding resonance spectral profile. The ER of the resonance at 156.76 GHz is 26 dB, which is the largest one in the spectrum and very close to the critical coupling. Figure 6(b) shows the result of this resonance with Q-factor of 201. The transmission spectrum response curve was fitted with Eq. (1.2). The fitted parameters are $n_{eff} = 2.8798$, $t = 0.858$, and $a = 0.842$ (~0.865 dB/cm), respectively. In order to further increase the resonance ER, t and a need to be in closer proximity to satisfy the critical coupling condition. The mode number retrieved from the finite difference time domain (FDTD) simulation is 26. The red-dash curve in Fig. 6(b) is the calculated spectrum using analytical model, which fits well to the experimental result. For the E_y^{11} mode, the transmission spectrum is shown in Fig. 6(c) by the blue-solid curve. We selected the resonance with Q-factor of 305 at $f = 194.6$ GHz, which is shown in Fig. 6(d) by the blue-solid curve. The ER of resonance is 23 dB. $n_{eff} = 2.855$, $t = 0.871$, and $a = 0.885$ (~0.614 dB/cm) can be obtained. The mode number is 32.The fitted transmission spectrum response is shown in Fig. 6(d) by the red-dash curve. It also fits well to the experimental data. The loss factor of the E_y^{11} mode is lower than that of E_x^{11} mode, which hence generates a high Q-factor resonance. Such experimental results verify the bending loss analysis in the section 2. According to the extracted parameters, t and a are key parameters for a high-Q resonance. The Q factor can be further increased by reducing waveguide bending and scattering loss through the larger radius and improved fabrication process. In Figs. 6(a) and 6(c), there is only one mode excited in the disk cavity, which we can deduce from the almost uniform free spectral range (FSR) and Q-factor features.

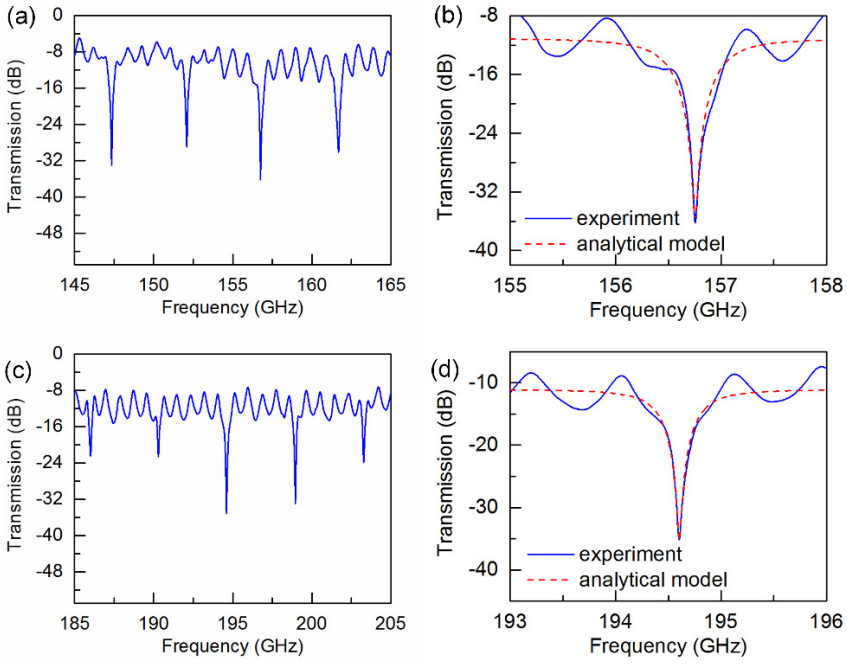

Fig. 6. Measured transmission spectra of the disk cavity device for (a) E_x^{11} mode and (c) E_y^{11} mode. Fitting results for (b) E_x^{11} mode and (d) E_y^{11} mode.

We further investigate the ring resonator in THz frequency range and obtain a high Q-factor resonator. The transmission spectrum of the racetrack ring is shown in Fig. 7(a) by the

Optical Materials EXPRESS

blue-solid curve for the E_x^{11} mode. The Q-factor of resonance at 189.4 GHz is 168, as shown in Fig. 7(b) in the blue-solid line. The ER reaches the maximum of 21.5 dB. n_{eff} = 2.9475, t = 0.7, and a = 0.729 (~0.679 dB/cm) are extracted parameters, respectively. The mode number retrieved from the simulation is 76. The calculated spectrum response is shown in Fig. 7(b) with the red-dash curve. Figure 7(c) shows the measured transmission spectrum for the E_y^{11} mode. We selected the resonance with Q-factor of 2839 at f = 218.345 GHz, which is shown in Fig. 7(d) by the blue-solid curve. n_{eff} = 2.89322, t = 0.978, and a = 0.975 (~0.054 dB/cm) can be obtained. The mode number is 87. The fitting result is shown in Fig. 7(d) by the red-dash curve. It also fits well to the experimental data.

Notably, the measured Q-factor of E_y^{11} mode of the racetrack ring is about nine times larger than that of the disk, that is mainly due to its larger cavity length, lower bending loss, and higher frequency. Moreover, we noticed another cause to such Q-factor difference: the uneven top surface roughness caused by over etching. Due to the out of flatness of photoresist and uneven deep silicon etching by the inductively coupled plasma (ICP) process, the roughness varies with different regions, as shown in Fig. 8. Observing through the microscope at a higher magnification (× 20), the disk surface obviously has larger roughness than the ring, which enlarges the gap between the Q-factors of the E_y^{11} mode in ring and disk.

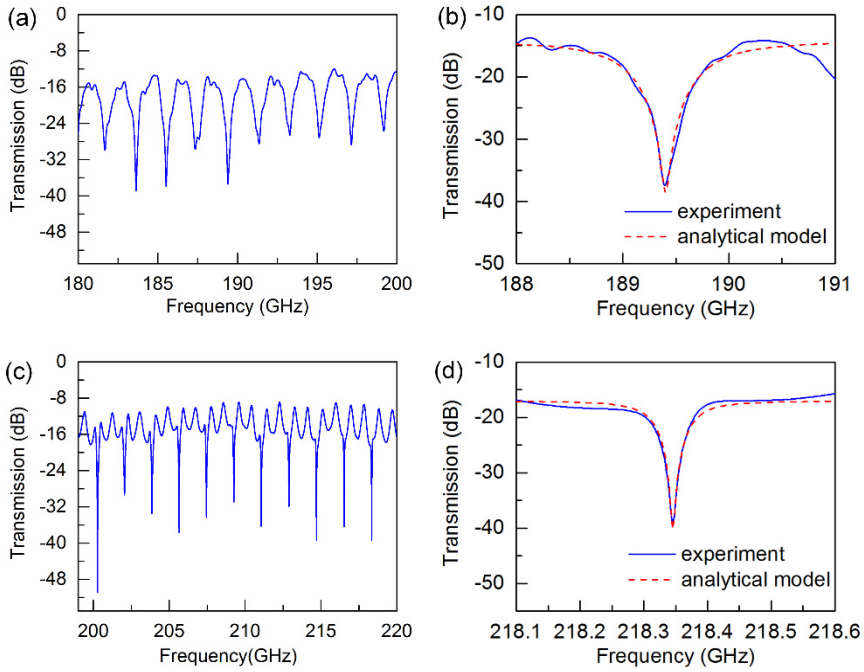

Fig. 7. Measured transmission spectra of the racetrack ring cavity device for (a) E_x^{11} mode and (c) E_y^{11} mode. Fitting results for (b) E_x^{11} mode and (d) E_y^{11} mode.

Optical Materials EXPRESS

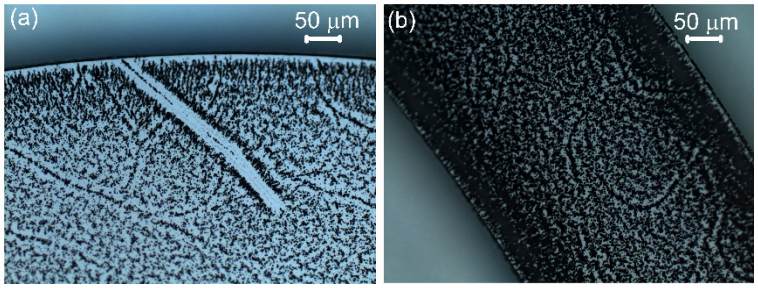

Fig. 8. Optical microscope images of (a) the disk and (b) the racetrack ring.

Table 1 lists the comparison of our racetrack ring with various state-of-the-art terahertz resonators including metasurfaces, metal plate waveguide, dielectric cavity, metal integrated cavity, photonic crystal. It can be seen the key merits of racetrack ring are the high Q-factor, small size, and high integratability.

Table 1. Comparison of Various Terahertz Resonators Obtained from Some Example Devices

	Q-factor	Frequency(GHz)	Device size(mm^2)	Integratability
Metasurfaces [15]	34.3	~550	>9.62	Low
Metal plate waveguide [11]	334	<450	large	Low
Dielectric cavity [18,19]	1600	350	28.27	Low
Metal integrated cavity [20]	65	1091	0.03	High
Photonic crystal [23]	1020	1072.4	72.6	High
Our work (racetrack ring)	2839	218.345	98.18	High

4. Conclusion

We proposed and experimentally demonstrated the compact THz silicon-based integrated cavities with high-Q factors. Both THz integrated whispering gallery mode in a disk resonator and high-Q racetrack ring resonator is demonstrated over a wide frequency range from 140 GHz to 220 GHz. Scattering and bending losses of the dielectric cavities are analyzed in numerical calculations. The results show that the waveguide and cavity losses of E_y^{11} modes is less than that of E_x^{11} modes. The experiment reveals that Q-factor of racetrack ring resonator can be significantly improved to 2839 for the E_y^{11} mode. Future work will concentrate on the design and fabrication optimization of the dielectric THz resonator.

Funding

National Natural Science Foundation of China (61705131, 11604208, 61671302, 61722111); Shanghai Sailing Program (16YF1407900); Natural Science Foundation of Shanghai (16ZR1445500, 16ZR1445600); National Program on Key Basic Research Project of China (973 Program) (2014CB339806); Major National Development Project of Scientific Instrument and Equipment (2017YFF0106300, 2016YFF0100503);Key Scientific and Technological Project of Science and Technology Commission of Shanghai Municipality (15DZ0500102); Shanghai Pujiang Program (17PJD028); Shanghai Leading Talent (2016-019); Young Yangtse River Scholar (Q2016212).